J. Fluid Mech. (2014), *vol.* 752, *pp.* 282–295.
doi:10.1017/jfm.2014.316

Intrusion-generated waves in a linearly stratified fluid

Benjamin D. Maurer and P. F. Linden†

Department of Applied Mathematics and Theoretical Physics, University of Cambridge, Cambridge CB3 0WA, UK

(Received 26 February 2013; revised 26 May 2014; accepted 2 June 2014; first published online 4 July 2014)

We present an experimental and numerical study of the upstream internal wavefield in a channel generated by constant density intrusions propagating into a linearly stratified ambient fluid during the initial phase of translation. Using synthetic schlieren imaging and two-dimensional direct numerical simulations, we quantify this wave motion within the ambient stratified fluid ahead of the advancing front. We show that the height of the neutral buoyancy surface in the ambient fluid determines the vertical modal response with the predominant waves being mode 2 for intrusions near the mid-depth of the channel and mode 1 waves being produced by intrusions nearer the top or bottom of the domain. All higher vertical modes travel slower than the intrusion and so do not appear upstream ahead of the intrusion front. We find the energy flux into this upstream wavefield to be approximately constant, and to be between 10 and 30 % of the rate of available potential energy transfer into the flow.

Key words: gravity currents, internal waves, stratified flows

1. Introduction

Intrusive gravity currents, or intrusions, are the buoyancy-driven flow of one fluid into another stratified fluid at an intermediate height. The intrusive flow sharpens horizontal density gradients, forming a front, which propagates laterally along an isopycnal surface. A common example occurs when the buoyant fluid in a plume rising in stably stratified surroundings reaches a height at which its density matches that of the ambient fluid, where it then spreads horizontally along the corresponding isopycnal surface as an intrusion. This kind of intrusion is exemplified by the speed of volcanic ash in the atmosphere or oil from a submarine release. In these cases, the stable stratification in the ambient fluid can support internal gravity waves (IGWs). We are interested in predicting their generation as the intrusion front moves and displaces isopycnal surfaces.

In this study we restrict our scope to the classic lock release, in which an intrusion is created in a rectangular channel by the sudden removal of a lock gate separating fluids of differing densities (figure 1). The fluids of height H are initially at rest in a channel of length L, with the gate positioned at L_{lock}. To the right of the gate, the density $\rho_a(z)$ of the ambient fluid decreases linearly with height from ρ_L to

† Email address for correspondence: p.f.linden@damtp.cam.ac.uk

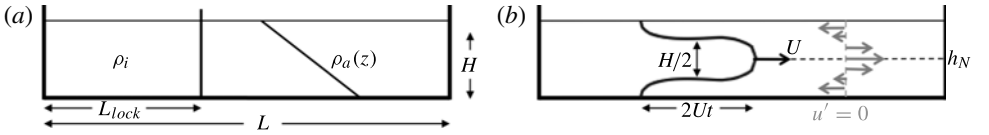

FIGURE 1. Schematic showing (*a*) the initial conditions of lock release, and (*b*) the resulting flow. The lock fluid of density ρ_i is separated by a gate from a stratified ambient fluid of density $\rho_a(z)$ and constant buoyancy frequency N. Once the gate has been removed, an intrusion travels with velocity U along the level h_N of neutral buoyancy generating an upstream-propagating disturbance.

ρ_U, implying a constant buoyancy frequency $N = \sqrt{-g(\rho_L - \rho_U)/\rho_0 H}$, where ρ_0 is a reference density. To the left of the gate, the intruding fluid has a constant intermediate density ρ_i, and $\rho_U \leqslant \rho_i \leqslant \rho_L$. When the gate is removed the intruding fluid is observed to accelerate into the ambient fluid before reaching a constant speed U, which is maintained for some time along its level h_N of neutral buoyancy, where the ambient isopycnal surface density matches that of the intrusion, $\rho_a(h_N) = \rho_i$ (Wu 1969; Manins 1976; Ungarish 2005; Bolster, Hang & Linden 2008; Maurer, Bolster & Linden 2010; Ungarish 2011).

Bolster *et al.* (2008) conducted full-depth lock releases in a channel containing a linearly stratified fluid at various levels of neutral buoyancy h_N. Using an ansatz based on the assumption that the available potential energy (APE) is converted at a constant rate into the kinetic energy of the intrusion, they predicted the intrusion speed U to be

$$U = \frac{F}{2}\left(3\left(\frac{H - 2h_N}{H}\right)^2 + 1\right)^{1/2} NH, \tag{1.1}$$

where $F \approx 0.25$ is the Froude number of an intrusion with $h_N = 0, H$ (i.e. a gravity current along the top or bottom of the channel with density equal to the ambient density at that height). The speed of the intrusion has a minimum $U = FNH/2$ at mid-depth, and increases quadratically to double that speed at the upper and lower boundaries of the fluid (Maxworthy *et al.* 2002; Ungarish & Huppert 2002).

The advance of the intrusion forces isopycnal perturbations in the ambient fluid, which may radiate as IGWs. Manins (1976) studied the upstream wavefield generated by a two-dimensional intrusion in a channel created by the constant volume flux injection of homogeneous fluid into a linearly stratified ambient fluid along a level of neutral buoyancy at the mid-depth. The intrusion initially travelled at a constant speed $U \sim Nh$, where the h is the intrusion thickness. In contrast to the waves generated by the transient adjustment studied by Wu (1969), the steadily forced intrusions generated horizontal, columnar internal wave modes within the ambient fluid, similar to those produced in experimental shear flow studies by McEwan & Baines (1974). IGWs propagating upstream were also observed in full-depth lock release experiments by Bolster *et al.* (2008), who commented on their existence but did not attempt to quantify their dynamics or energetics. They showed, however, that all intrusions are subcritical with respect to IGWs which transfer energy and momentum to the ambient fluid and modify the upstream stratification.

In this paper we focus on these waves that propagate upstream ahead of the intrusion. In the case of a two-layer ambient fluid Cheong, Kuenen & Linden (2006)

showed that, in general, an interfacial wave propagated upstream and altered the height of the interface ahead of the intrusion, modifying its propagation speed (Flynn & Linden 2006). Internal waves are also generated behind the front of the intrusion, both by the intrusion itself and also by interactions of the flow into the lock with the rear wall of the lock. In a study focused on the effects of finite-length locks, Munroe *et al.* (2009) found that there can be strong interactions between the intrusion and the waves reflected from the back of the lock. In some cases these interactions are sufficient to stop the intrusion propagating. These reflected waves are the analogue of the finite-amplitude bore generated by reflections from the end wall in a lock-release gravity current. In that case the bore overtakes the current and is responsible for the transition from the constant-velocity phase to the similarity phase (Rottman & Simpson 1983).

In the continuously stratified case these reflected waves, resulting from short locks (length-to-height aspect ratio $L_{lock}/H \lesssim 1$), can cause large distortions of the intrusion (see figures 2–5 in Munroe *et al.* 2009) and influence the propagation speeds, Since we are motivated by environmental flows where finite locks are not relevant, our study is restricted to the case where $L_{lock}/H = 2$ so that the reflected waves did not affect the motion of the front of the intrusion, which was observed to travel at a constant speed until interacting with the far end wall of the tank. This provides a closer representation of intrusions generated by features such as plumes or frontal instabilities. We are concerned here only with waves that propagate ahead of the intrusion, as they modify the stratification into which the intrusion is moving. While other waves are generated that travel more slowly than the intrusion and are left behind the advancing front, they are not the subject of this study.

The fastest linear IGWs in a channel with constant buoyancy frequency N are columnar modes that travel horizontally with speeds c_m that decrease as a function of their vertical mode number m (McEwan & Baines 1974), and are given by

$$\frac{c_m}{NH} = \frac{1}{m\pi}, \quad m = 1, 2, 3, \ldots. \tag{1.2}$$

Note that both the intrusion speed (1.1) and the speeds of the wave modes (1.2) scale linearly with NH and $U < c_1$. Hence, all intrusions are subcritical to mode 1 linear columnar long waves for all levels of neutral buoyancy $0 \leqslant h_N \leqslant H$, whereas mode 2 waves can propagate upstream only when $U < c_2$ (see also Bolster *et al.* 2008, figure 4). This occurs for intrusions near the mid-depth of the channel with $h_2^- < h_N < h_2^+$, where

$$h_2^{\pm} = \frac{H}{2}\left(1 \pm \sqrt{\frac{1}{3}\left(\frac{1}{\pi^2 F^2} - 1\right)}\right), \tag{1.3}$$

yielding $h_2^- = 0.27H$ and $h_2^+ = 0.73H$ for $F = 0.25$. Finally, $c_m < U$ for $m \geqslant 3$ and, therefore, all intrusions are supercritical to mode 3 and higher modes, and these waves do not radiate upstream.

This study aims to understand the structure and energetics of the upstream IGW motion generated by high-Reynolds-number, Boussinesq intrusions in a linearly stratified ambient fluid, during the initial constant-velocity phase of propagation. In § 2, we describe the laboratory experiments and the two-dimensional direct numerical simulation (DNS) methodology. We present the observed structure and propagation speeds of the IGWs and the associated energy fluxes in § 3. In § 4, we present our conclusions and discuss the implications of this study for propagation of intrusive gravity currents into a linearly stratified ambient fluid.

2. Methods

2.1. *Laboratory experiments*

Laboratory experiments were conducted in a channel for five values of neutral buoyancy levels $h_N/H = \{0.09, 0.21, 0.31, 0.42, 0.47\} \pm 0.02$ in an ambient fluid of (fixed) constant buoyancy frequency $N = 0.96 \pm 0.01$ s^{-1}. The minimum Reynolds number $Re \equiv NH^2/\nu$ for these flows was $Re = 3.8 \times 10^4$, indicating that viscous forces were negligible.

The experimental channel was 183 cm long, 23 cm wide, and 30 cm high, and filled with salt water (Schmidt number, $Sc = \nu/\kappa \approx 10^3$) to a depth $H = 20 \pm 0.1$ cm using the double-bucket method (Oster 1965; Economidou & Hunt 2009) and sponge floats to create a linear stratification. Once the tank had been filled it was divided by adding a vertical gate at a distance $L_{lock} = 40$ cm from one end-wall of the tank. As discussed in the Introduction, the length of the lock $L_{lock} = 2H$ was set such that waves reflected from the rear of the lock have insufficient time to reach the front before the mode 1 wave reaches the upstream far end-wall of the tank. With the gate in place, the lock fluid was stirred to homogenise the density and additional salt was added to attain the appropriate value of the intrusion density ρ_i. The buoyancy frequency N of the ambient fluid was determined by drawing water samples with a syringe every 4 cm over the height of the fluid and measuring the sample densities with an Anton–Paar 5000 DMA density meter (accuracy of 10^{-6} g cm^{-3}).

Images of the flow were recorded with a CCD camera (model Jai CV − M4 + CL) at 1390 × 1024 pixel resolution, yielding approximately 0.17 cm pixel^{-1} spatial resolution. The camera was positioned normal to the front wall of the channel at a distance of 5.67 m. The experiment was illuminated by a vinyl light sheet located 42 cm beyond the back wall of the channel. An opaque mask, with randomly distributed transparent dots 0.15 cm in diameter and an average distance of 0.45 cm apart, was placed directly in front of the light sheet (Dalziel, Hughes & Sutherland 2000). The vertical spacing was chosen to allow the capture of IGW amplitudes an order of magnitude smaller than the maxima of $H/5$ observed by Munroe *et al.* (2009). The camera, channel and light sheet were placed beneath a large plastic cover to isolate them from time varying density gradients in the air. Images of the channel and mask were recorded directly onto a PC via Digiflow software (Dalziel 2004) at 24 frames s^{-1}. Experimental images were taken only until the theoretical first arrival of the mode 1 internal wave at the upstream wall at time $t = \pi(L - L_{lock})/NH$, preventing the possibility of reflected internal wave motion in the upstream measurement volume.

Using the synthetic schlieren processing package within Digiflow, apparent shifts in the image of the mask of random dots were inverted along a light ray path to yield the vertical gradient of the perturbation density field $\partial\rho'/\partial z$ (Dalziel 2004). From this field, the perturbations to the square of the buoyancy frequency were computed as $\Delta N^2 = (-g/\rho_0)(\partial\rho'/\partial z)$. Successive images were then averaged over 0.5 s, or approximately 1/12 of the minimum internal wave period, to reduce noise in the images. The homogenous density field within the intrusion is identified by ΔN^2, and the intrusion front was determined to be the upstream-most horizontal position where $\Delta N^2(x, z)/N_a^2 < -0.90$ (see figure 2). The intrusion speed is then estimated by tracking the identified front through successive frames (Shin, Dalziel & Linden 2004). The downstream limit of the ambient fluid control volume is also defined by this front position.

From measurements of ΔN^2 within the ambient fluid, we recover the vertical isopycnal displacement $\zeta'(x, z, t)$, the vertical velocity $w'(x, z, t)$ and horizontal velocity $u'(x, z, t)$ fields by linear theory:

$$\zeta' = -\frac{1}{N^2}\int \Delta N^2 \,\mathrm{d}z, \quad w' = -\frac{1}{N^2}\int \frac{\partial(\Delta N^2)}{\partial t}\,\mathrm{d}z, \quad u' = \frac{1}{N^2}\int \frac{\partial(\Delta N^2)}{\partial t}\,\mathrm{d}x. \quad (2.1a\text{–}c)$$

All integrals were evaluated using Simpson's rule, and time derivatives were taken as the first-order backward difference across successive (0.5 s averaged) video frames.

2.2. *Numerical simulations*

Two-dimensional DNS of lock releases, corresponding to the laboratory experiments, were conducted for five equally spaced values of the neutral buoyancy level h_N/H between 0.10 and 0.50 at a background ambient buoyancy frequency $N = 1.0$ s^{-1}. The minimum Reynolds number for the simulations was $Re = 4 \times 10^4$.

The simulations were conducted in a two-dimensional domain, composed of two symmetric lock releases with equal dimensions to the laboratory tank (183 cm $\times$ 20 cm), reflected about a vertical line of symmetry with the lock fluid propagating from the centre outwards (Sutherland, Flynn & Dohan 2004). The numerical domain was discretised into a uniform grid of 1024×256 points, yielding a vertical grid spacing of $\Delta x = 0.078$ cm, much smaller than the maximum upstream isopycnal displacement observed by Munroe *et al.* (2009) of $H/5$. The lock fluid occupied $L_{lock} = 40$ cm in each of the two numerical domains and was marked with a passive tracer.

A slightly modified version of the open-source DNS algorithm Diablo (Taylor 2008) was used to solve the two-dimensional, incompressible, Boussinesq Navier–Stokes equations subject to no-slip boundary conditions on rigid top and bottom surfaces, with kinematic viscosity $\nu = 0.01$ cm^2 s^{-1} and Schmidt number $Sc = 1$. The horizontal symmetry allowed periodic boundary conditions at the ends of the channel and, therefore, the spectral evaluation of flow variables in the horizontal direction. To minimize Gibbs phenomena, initial density steps in the horizontal direction were smoothed with a hyperbolic tangent profile. The flow was advanced with a combination of a third-order, low-storage Runge–Kutta–Wray scheme and a Crank–Nicholson scheme at $\Delta t = 0.001$ s. Vertical derivatives were evaluated using second-order centred finite differences. Only vertical diffusive terms were treated implicitly.

The flow was set into motion and the calculations continued until the mode 1 waves reached the ends of the domain at $t = \pi(L - L_{lock})(NH)^{-1}$. Field information for density ρ, velocity $\boldsymbol{u}$ and tracer concentration C was recorded at 0.5 s intervals over the entire domain for the duration of the simulation. The position of the intrusion front was determined to be the upstream-most point where the concentration, C was 95 % of the initial lock concentration (see figure 5). This threshold value is more precise than used in experiments as the laboratory data were more noisy. However, comparisons between corresponding experiments and simulations showed that the outlines of the intrusion edge were consistent. The front position was also taken to be the downstream limit of the upstream ambient fluid control volume. Tracking the front position through successive frames provided a measure of the intrusion speed.

2.3. *Post-processing*

To identify individual IGW modes, the upstream isopycnal displacement ζ' and perturbation velocity fields w' and u' for each frame were decomposed into vertical

modes

$$\hat{u}'_m(x) = \frac{2}{H}\int_0^H u'(x,z)\cos\left(\frac{m\pi z}{H}\right)\mathrm{d}z, \tag{2.2}$$

$$\hat{w}'_m(x),\,\hat{\zeta}'_m(x) = \frac{2}{H}\int_0^H w'(x,z),\,\zeta'(x,z)\sin\left(\frac{m\pi z}{H}\right)\mathrm{d}z, \tag{2.3}$$

so that the vertical velocity is zero at the upper and lower boundaries. Fourier decomposition gives the local modal coefficients $\hat{\zeta}'_m(x)$, $\hat{w}'_m(x)$ and $\hat{u}'_m(x)$ describing the maximum magnitude of the displacement, vertical and horizontal velocity components as functions of x. Constructing $x-t$ diagrams from time series of these coefficients gave the wave speed c_m as the slope of the boundary between the perturbed and quiescent fluid, taken to be 10 % of the maximum $\hat{\zeta}'_m(x)$, $\hat{w}'_m(x)$ or $\hat{u}'_m(x)$ for a given m within the control volume at that time t. This boundary was observed to be straight on the $x-t$ plots, showing that the wave speeds were constant.

The wavefield properties were then recomposed via the appropriate basis functions, retaining only modes $0<m<5$, effectively band-pass filtering the data. This removed the fundamental mode associated with the seiching (mode 0) caused by the surface waves in the experiments and higher-frequency noise ($m>5$) generated by the synthetic schlieren processing of the laboratory images or by the spectral solver within the numerical data. This allowed for a more accurate estimation of the wave energy within the control volume upstream of the current:

$$E_{P,m}(t)=\frac{1}{2}\int_V \rho_0 N^2\zeta'^2\,\mathrm{d}V, \quad E_{K,m}(t)=\frac{1}{2}\int_V \rho_0(u'^2+w'^2)\,\mathrm{d}V, \tag{2.4a,b}$$

describing the total potential energy $E_{P,m}(t)$ and total kinetic energy $E_{K,m}(t)$, respectively, of a given mode m within the control volume. For linear waves we expect equipartition between the potential and kinetic energy for a given mode.

The rate at which APE is transferred into the flow was estimated by the rate of change of the initial stratification. The APE of the initial configuration of the lock-release of a well-mixed fluid released into a linearly stratified ambient fluid per unit horizontal area is (Ungarish & Huppert 2006)

$$E_{APE}=\tfrac{1}{6}g((\rho_L-\rho_i)h_N^2+(\rho_i-\rho_U)(H-h_N)^2). \tag{2.5}$$

As the current advances at speed U and occupies approximately half the fluid depth, continuity requires that the boundary currents moving into the lock region are also advancing at an average speed U. Therefore, to a first approximation, the rate of conversion of APE into the kinetic energy of the flow is $2UE_{APE}$. Although this rate of APE release is approximate it is consistent with energy-conversion approaches used in gravity current lock exchanges (Yih 1947, 1965), and it provides a convenient baseline for the energetics of the flow. The relative fluxes of potential and kinetic energies, respectively, into the upstream control volume for a given wave mode normalised by the power supplied by the conversion of APE are given by the dimensionless quantities

$$P_m,\,K_m=\frac{(\mathrm{d}/\mathrm{d}t)(E_{P,m},\,E_{K,m})}{2UE_{APE}}. \tag{2.6}$$

3. Results

3.1. *Qualitative observations*

Figures 2 and 3 show experimental and numerical results for intrusions with neutral levels $h_N \sim 0.1H$ near the bottom of the channel, at $Nt = 15.5$. By this time the intrusions have propagated a little over two lock lengths and there is good agreement between the front positions for the experiments and the simulations. This agreement in intrusion speeds even for two-dimensional calculations is a common feature of these flows and gravity currents (Bolster *et al.* 2008), implying that the bulk dynamics is essentially independent of the channel width. The isopycnals in figure 3(*a*) are observed to be lifted above the oncoming intrusion, and at the level of the intrusion the flow in the ambient fluid is forward while above the intrusion there is reverse flow indicative of a mode 1 response. This structure can also be seen in the perturbation N^2 field in figure 2(*a*). The modal responses for the experiment and the simulation are shown in figures 2(*b*) and 3(*b*), respectively. These show a predominant mode 1 response with almost no signal in mode 2.

The mode 1 wave has propagated ahead of the intrusion as expected and shows agreement between the experiment and the simulation. The difference in speeds between the intrusion and the wave implies that the region of upstream disturbance increases with time. However, the maximum value of the mode strength was not observed to change with time and is associated with the displacement of the isopycnals at the front of the intrusion, which remains constant as the intrusion propagates. The time evolution of these fields and the mode strengths can be seen in the movies in the supplementary material available at http://dx.doi.org/10.1017/jfm.2014.316.

Figures 4(*a*) and 5(*a*) show experimental and numerical results for intrusions at mid-depth, at $Nt = 15.5$. These images show that at this time they have both propagated one lock length from the gate, about half the speed of an intrusion near the bottom of the channel, as expected. The laboratory image (figure 4*a*) shows the intensification of the density gradient above and below the intrusion. Figure 5(*a*) shows also the intensification of the density gradient near the top and bottom boundaries. Ambient fluid is pushed forward in front of the intrusion and there is a reversed flow near the top and bottom boundaries. This motion is characteristic of a mode 2 IGW, which is also consistent with the observed distortion of the isopycnals. The vertical mode strengths, calculated from (2.3) are shown in figures 4(*b*) and 5(*b*). The laboratory intrusion has transmitted energy to both mode 1 and mode 2 waves, with the majority in mode 2, while the vertically symmetric simulation projects only on to mode 2. The values of the mode 2 strengths are similar in both cases, and independent of time as they are again set by the flow over the intrusion front, and the waves have propagated ahead of the intrusion by similar distances (about one-half a lock length) in both cases.

These results are consistent with the discussion of wave speeds that show that all intrusions are subcritical to mode 1 waves, while only those near the mid-depth of the channel are subcritical to mode 2 waves. No evidence was found of significant energy in modes 3 and higher, again consistent with the earlier discussion. Comparisons over the full range of neutral level depths between experiments and simulations are given in figure 6, which shows the intrusions and the isopycnals upstream at $Nt = 10$ for $h_N/H \approx 0.1, 0.3$ and 0.5. There is good qualitative and quantitative agreement between the experiments and the DNS. Although not shown here, the intrusions were observed to propagate at constant speeds, and both experiments and simulations are found to be in agreement with the energy ansatz of Bolster *et al.* (2008), (presented as (1.1)

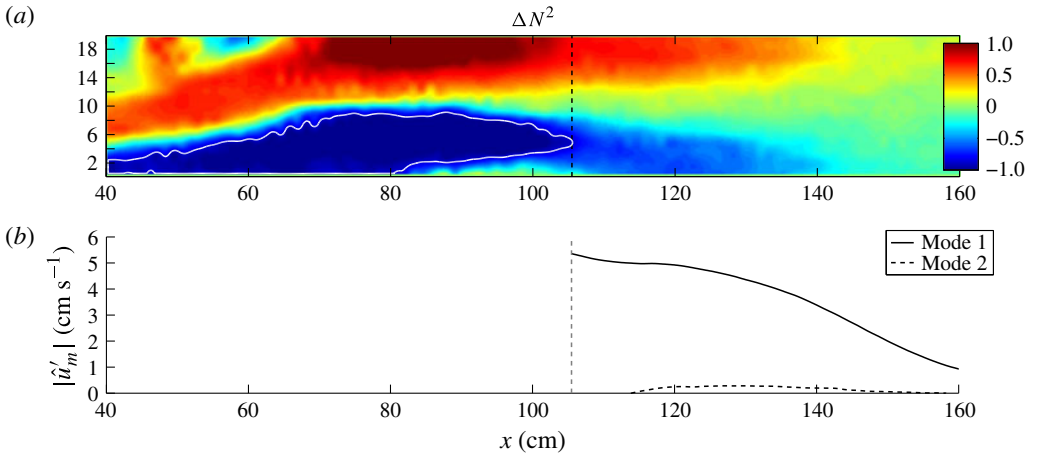

FIGURE 2. (*a*) An image of the experiment for $h_N = 0.09H$ at $Nt = 15.5$. The perturbation buoyancy frequency field ΔN^2 is overlain by a white solid contour of $\Delta N^2 = -0.90N_a^2$, which marks the edge of the intrusion and, therefore, the start of upstream control volume which is demarcated by the vertical dashed black line. Within this control volume, perturbations to the buoyancy frequency field are shown in colour over the range $-1.0 \leqslant \Delta N^2/N_a^2 \leqslant 1.0$, ranging from dark blue to dark red, respectively. (*b*) A plot of the absolute value of the vertical mode strength of the horizontal component of velocity $\hat{u}'_m$, given by (2.2), for mode 1 and mode 2 at each position x in the upstream control volume.

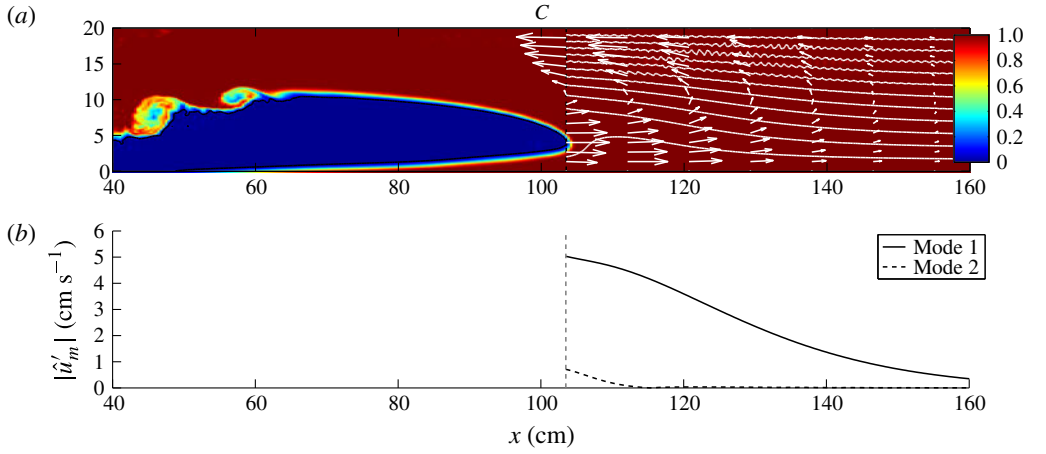

FIGURE 3. (*a*) An image of the numerical simulation of $h_N = 0.1H$ at $Nt = 15.5$. The tracer concentration field is overlain by a white solid contour of $C > 95\,\%$, the front position and therefore the upstream control volume is demarcated by the black vertical dashed line. Within the control volume, density contours are drawn every 0.002 g cm^{-3}, and velocity field magnitudes and directions are given as arrows. (*b*) A plot of the absolute value of the vertical mode strength of the horizontal component of velocity $\hat{u}'_m$ given by (2.2) for mode 1 and mode 2 at each position x in the upstream control volume.

in this paper). These speeds imply the intrusions are faster than IGWs with vertical mode $m \geqslant 3$, and those waves that are observed to propagate ahead of the intrusion consist of a superposition of mode 1 and mode 2 disturbances.

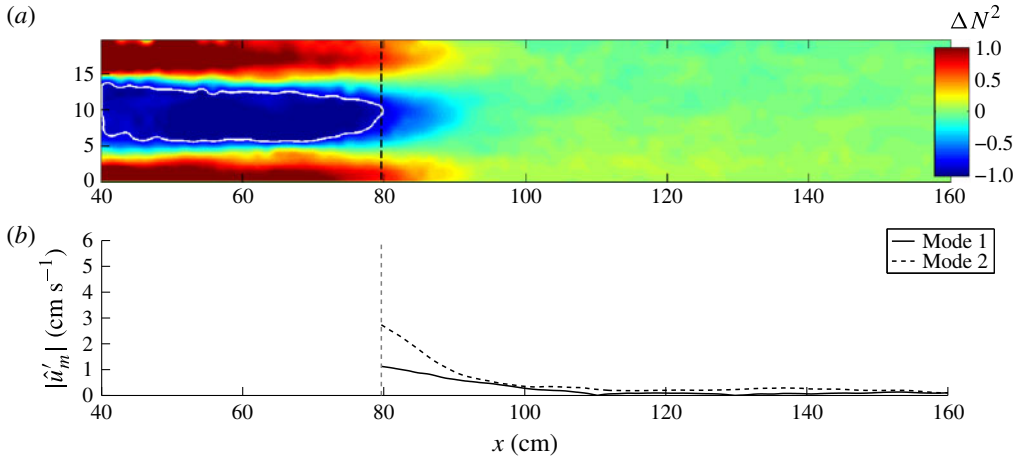

FIGURE 4. (*a*) An image of the experiment for $h_N = 0.47H$ at $Nt = 15.5$. The colours etc. are the same as in figure 2. (*b*) A plot of the absolute value of the vertical mode strength of the horizontal component of velocity $\hat{u}'_m$, given by (2.2), for mode 1 and mode 2 at each position x in the upstream control volume.

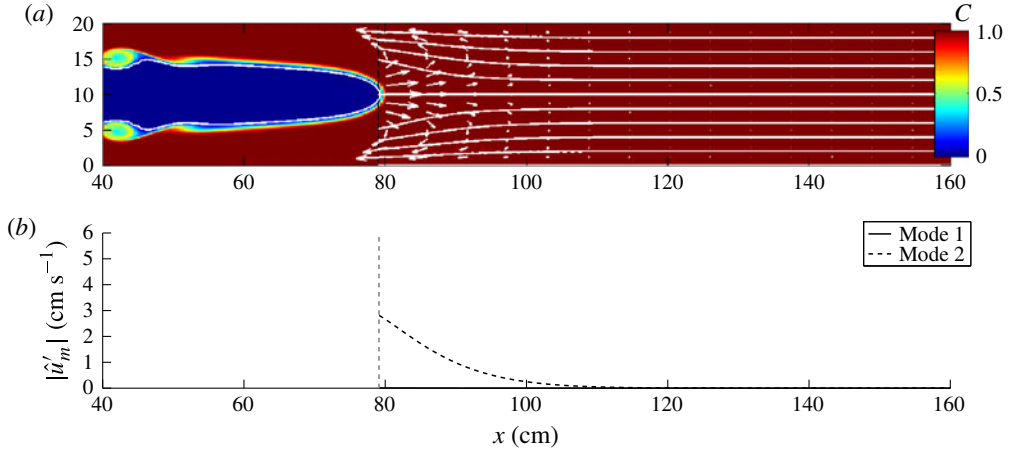

FIGURE 5. (*a*) An image of the numerical simulation of $h_N = 0.50H$ at $Nt = 15.5$. The contours are the same as in figure 3. (*b*) A plot of the absolute value of the vertical mode strength of the horizontal component of velocity $\hat{u}'_m$ given by (2.2) for mode 1 and mode 2 at each position x in the upstream control volume.

The mid-height intrusions, shown in figure 6(*a*,*b*), travel the slowest and generate elevation and depression of the upstream isopycnals symmetrically about the mid-plane. This IGW motion is consistent with a mode 2 signal. Near-bottom-boundary intrusions, shown in figure 6(*e*,*f*), travel faster and generate only elevations consistent with a mode 1 IGW signal. The intermediate intrusions just above the condition $h_2^-/H = 0.27$ (1.3) at which mode 2 waves are faster than the intrusion, shown in figure 6(*c*,*d*), exhibit an asymmetric depression and elevation of isopycnals consistent with a superposition of mode 1 and mode 2 signals.

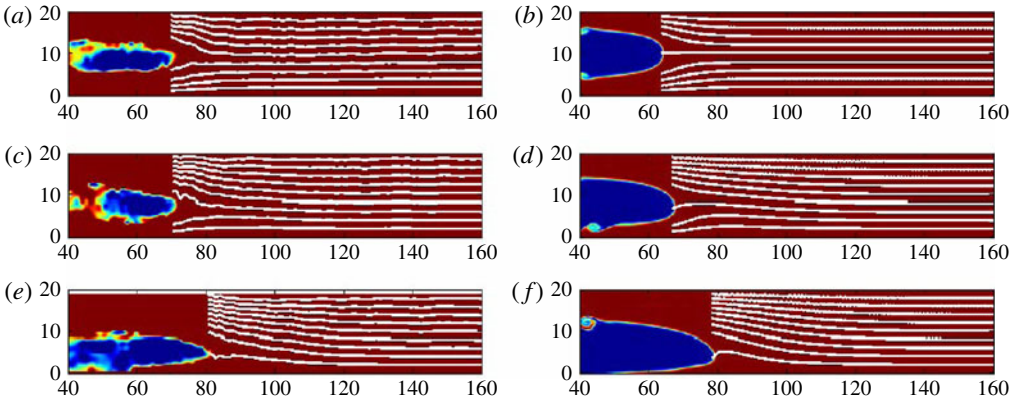

FIGURE 6. Images of the intrusions and corresponding density fields at $Nt = 10$ for selected laboratory experiments, (*a*) $h_N = 0.47$, (*c*) 0.31 and (*e*) 0.09, and numerical simulations, (*b*) $h_N = 0.50$, (*d*) 0.30 and (*f*) 0.10.

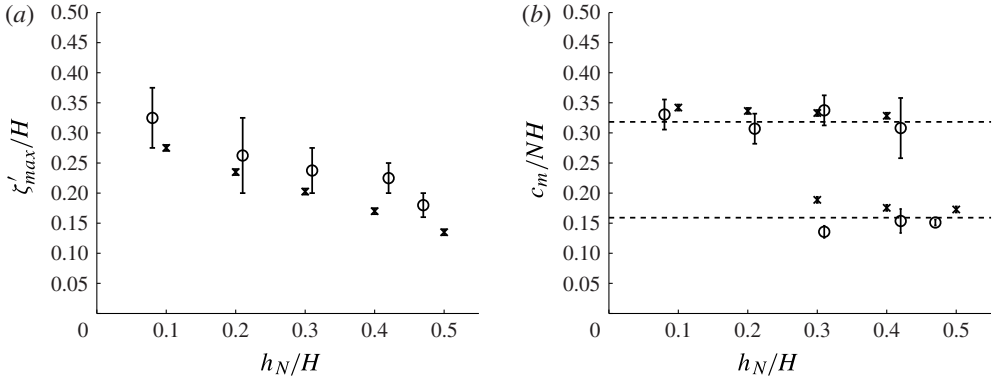

FIGURE 7. A plot of the maximum isopycnal displacement (*a*) and the columnar mode speed (*b*) versus level of neutral buoyancy, showing both experimental (○) and numerical (×) results. The error bars represent the standard deviation about a least-squares fit to the data.

3.2. *Quantitative observations*

Measurements of the upstream wavefields were used to calculate the amplitudes and speeds of the waves. As discussed in § 3.1 the wave amplitudes were largest near the intrusion and decayed monotonically with distance upstream of the front. The maximum isopycnal displacement ζ'_{max} within the control volume over time t is shown in figure 7(*a*). Although there is some variation with the level of neutral buoyancy, the maximum displacements, which occur near the front of the intrusion, are approximately one-third of the total fluid depth H or less. This displacement is consistent with the flow passing over and under the advancing intrusion. The upstream amplitudes $\hat{\zeta}'(x)$ for all times t monotonically approach zero as x increases upstream, implying a wavelength λ that is much greater than the length of the experiment (see figure 6). This very low isopycnal slope, $\hat{\zeta}'(x)/\lambda \lesssim 0.05$ is indicative of linear IGWs.

These values of the wave amplitude are significantly (about a factor of two) higher than those observed by Munroe *et al.* (2009), and described by their empirical formula

(3.10) in that paper. The reasons for this difference are not clear, although as pointed out above the initial configurations are different and the resulting intrusions propagate quite differently, with those presented here propagating at a constant velocity over the measurement period.

Figure 7(*b*) presents the speeds of the radiated internal wave modes, calculated by tracking the upstream extent of the amplitude of $\hat{\zeta}'_m(x) \geqslant 0.1\zeta'_{max}$. Measurements of mode 1 disturbances for mid-plane intrusions were omitted, as there was insufficient signal to determine wave speed. Similarly, mode 2 disturbances were only tracked for intrusions where $h_N > h_2^- = 0.27H$, below which neutral height the intrusion was supercritical to this wave mode. The measured wave speeds c_1 and c_2 are the same in every case, independent of h_N, and there is good agreement between experiments and numerical simulations. The speeds shown are close to the linear long-wave speeds (1.2), shown as the dashed black lines for both mode 1 and mode 2. This level of agreement suggests that the horizontal wavelength exceeds 100 cm, which is consistent with the monotonic decay in amplitude upstream of the intrusion.

For intrusions at all levels of neutral buoyancy, we observed a linear increase with time in the potential, kinetic, and total wave energy within the control volume, as calculated by (2.4*a*,*b*), prior to the arrival of the wave at the upstream end wall. Figure 8 presents the dimensionless rates of APE transferred to the upstream wavefield, calculated from (2.6). Figure 8(*a*–*d*) show the relative transfer rate of mode 1 and mode 2 potential and kinetic energy, respectively, in the upstream control volume as a proportion of the APE conversion rate. There is close agreement between the experiments and the numerics with the exception of P_1, where the laboratory values are significantly higher. Approximate equipartition between kinetic and potential energy is observed for individual modes, although again the experiments show larger values of P_1 than K_1: the reasons for this inconsistency are not clear. As expected, intrusions near the bottom boundary transfer more energy to mode 1 than mode 2 (figure 6*e*,*f*), while the opposite is true as the intrusion nears the mid-plane (figure 6*a*,*b*). The total rate of energy transfer ($P_m + K_m$) radiated to the upstream control volume is less than approximately 30 % of the APE released into the flow.

4. Discussion and conclusions

This paper has examined the structure and energetics of the upstream internal wavefields generated by well-mixed intrusive gravity currents propagating into a linearly stratified ambient fluid. Using laboratory experiments and two-dimensional numerical simulations, we have examined the internal wave response over the range of neutral buoyancy levels $0.1 \leqslant h_N/H \leqslant 0.5$. As the flow is Boussinesq, we expect the behaviour for intrusions above the mid-plane to behave symmetrically as they depart from the equilibrium condition $h_N/H = 0.5$.

Measured intrusion speeds varied with level of neutral buoyancy h_N as described by (1.1) (Bolster *et al.* 2008). All intrusions were observed to be subcritical to theoretical linear IGW mode 1 waves, while intrusions within $h_2^{\pm}$ described in (1.3) were observed to also be subcritical to mode 2. These intrusions generated a IGW response well-described by hydrostatic linear wave theory: low-amplitude isopycnal disturbances, constant group velocities, an equipartitioning of energy between potential and kinetic energy fields, and agreement with shallow-water wave speeds described in (1.2). As noted by Manins (1976), this agreement implies that the angle of wave energy propagation is approximately horizontal, consistent with steady (zero frequency) forcing of the wavefield by the steadily propagating current.

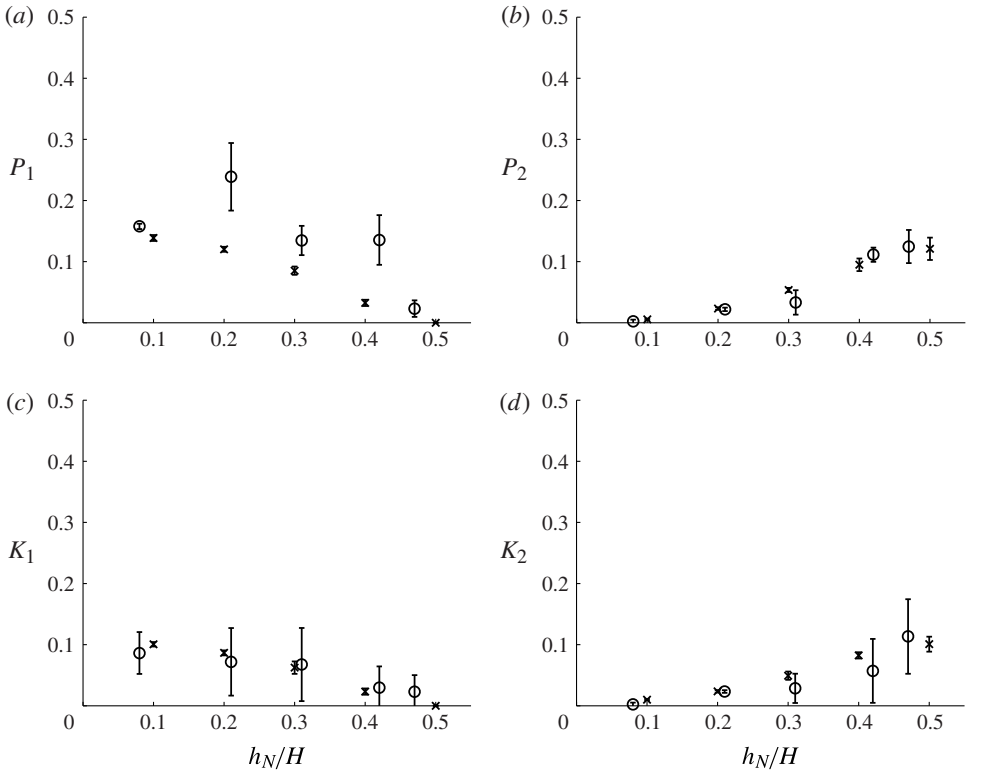

FIGURE 8. Measured rate of change of mode 1 (P_1, K_1) and mode 2 (P_2, K_2) potential and kinetic energy, respectively, normalised by the estimated rate of energy transfer from the initial APE (2.6) within the upstream control volume for experiments (○) and simulations (×). The error bars represent the standard deviation about a least-squares fit to the data.

Measurements of IGW potential and kinetic energy for individual modes show a strong influence of the level of neutral buoyancy on the relative proportion of energy transferred to the different vertical wave modes (figure 8). This proportion is a function of the level of neutral buoyancy h_N of the intrusion. Intrusions at the mid-plane are slow enough to radiate mode 2 IGWs and have forcing at a height that projects on to the mode 2 horizontal velocity profile. Although they are also subcritical to mode 1 IGWs, the projection on to the mode 1 horizontal velocity component profile is low; as a result, there is no energy transferred to the mode 1 wavefield. Conversely, near-bottom-boundary intrusions transfer energy only into mode 1. This is due to both the intrusions being supercritical to the mode 2 group speed and also the location of forcing near a null of the mode 2 horizontal velocity profile. In between these extremes energy is projected onto both modes 1 and 2. There is no evidence of significant energy at higher vertical mode numbers.

Our observations of the intrusion-generated wavefield show a constant transfer rate of approximately 10–30 % from APE into wave energy. These values are similar to those found for intrusions generated by short locks and which are influenced by IGWs reflected from the rear wall of the lock (Munroe *et al.* 2009). The waves distort the ambient density field in each case reducing the local N^2 immediately

ahead of the front of the intrusion. It seems that this reduction in the density gradient compensates for the loss of energy to the waves, so that the intrusion propagates at a speed independent of this energy loss (Ungarish & Huppert 2002; Bolster *et al.* 2008).

Acknowledgement

This research was supported by the National Science Foundation (grant number CTS-0756396).

Supplementary material

Supplementary material is available at http://dx.doi.org/10.1017/jfm.2014.316.

REFERENCES

BOLSTER, D. T., HANG, A. & LINDEN, P. F. 2008 The front speed of intrusions into a continuously stratified medium. *J. Fluid Mech.* **594**, 369–377.

CHEONG, H. B., KUENEN, J. J. P. & LINDEN, P. F. 2006 The front speed of intrusive gravity currents. *J. Fluid Mech.* **552**, 1–11.

DALZIEL, S. B. 2004 *Digiflow Manual*, 1st edn Dalziel Research Partners.

DALZIEL, S. B., HUGHES, G. O. & SUTHERLAND, B. R. 2000 Whole-field density measurements by 'synthetic schlieren'. *Exp. Fluids* **28**, 322–335.

ECONOMIDOU, M. & HUNT, G. R. 2009 Density stratified environments: the double-tank method. *Exp. Fluids* **46**, 453–466.

FLYNN, M. R. & LINDEN, P. F. 2006 Intrusive gravity currents. *J. Fluid Mech.* **568**, 193–202.

MANINS, P. C. 1976 Intrusion into a stratified fluid. *J. Fluid Mech.* **74**, 547–560.

MAURER, B. D., BOLSTER, D. T. & LINDEN, P. F. 2010 Intrusive gravity currents between two stably stratified fluids. *J. Fluid Mech.* **647**, 53–69.

MAXWORTHY, T., LEILICH, J., SIMPSON, J. E. & MEIBURG, E. H. 2002 The propagation of a gravity current into a linearly stratified fluid. *J. Fluid Mech.* **453**, 371–394.

MCEWAN, A. D. & BAINES, P. G. 1974 Shear fronts and an experimental stratifed shear flow. *J. Fluid Mech.* **63**, 257–272.

MUNROE, J. R., VOEGELI, C., SUTHERLAND, B. R., BIRMAN, V. & MEIBURG, E. H. 2009 Intrusive gravity currents from finite length locks in a uniformly stratified fluid. *J. Fluid Mech.* **635**, 245–273.

OSTER, G. 1965 Density gradients. *Sci. Am.* **213**, 70–76.

ROTTMAN, J. W. & SIMPSON, J. E. 1983 Gravity currents produced by instantaneous release of a heavy fluid in a rectangular channel. *J. Fluid Mech.* **135**, 95–110.

SHIN, J. O., DALZIEL, S. B. & LINDEN, P. F. 2004 Gravity currents produced by lock exchange. *J. Fluid Mech.* **521**, 1–34.

SUTHERLAND, B. R., FLYNN, M. R. & DOHAN, K. 2004 Internal wave excitation from a collapsing mixed region. *Deep-Sea Res.* II **51** (25–26), 2889–2904.

TAYLOR, J. R. 2008 Numerical simulations of the stratified oceanic bottom boundary layer. PhD thesis, University of California, San Diego.

UNGARISH, M. 2005 Intrusive gravity currents in a stratified ambient: shallow-water theory and numerical results. *J. Fluid Mech.* **535**, 287–323.

UNGARISH, M. 2011 Gravity currents and intrusions of stratified fluids into a stratified ambient. *Environ. Fluid Mech.* **12** (2), 115–132.

UNGARISH, M. & HUPPERT, H. E. 2002 On gravity currents propagating at the base of a stratified ambient. *J. Fluid Mech.* **458**, 283–301.

UNGARISH, M. & HUPPERT, H. E. 2006 Energy balances for propagating gravity currents: homogeneous and stratified ambients. *J. Fluid Mech.* **565**, 363–380.

WU, J. 1969 Mixed region collapse with internal wave generation in a density stratified medium. *J. Fluid Mech.* **35**, 531–544.

YIH, C. S. 1947 A study of the characteristics of gravity waves at a liquid interface. Master's thesis, State University of Iowa.

YIH, C. S. 1965 *Dynamics of Nonhomogeneous Fluids*. Macmillan.